Journal of Coastal Research	17	4	919–930	West Palm Beach, Florida	Fall 2001

Obliquely Incident Wave Reflection and Runup on Steep Rough Slope

Nobuhisa Kobayashi and Entin A. Karjadi

Center for Applied Coastal Research
University of Delaware
Newark, DE 19716

ABSTRACT

KOBAYASHI, N. and KARJADI, E.A., 2001. Obliquely incident wave reflection and runup on steep rough slope. *Journal of Coastal Research,* 17(4), 919–930. West Palm Beach (Florida), ISSN 0749-0208.

A two-dimensional, time-dependent numerical model for finite amplitude, shallow-water waves with arbitrary incident angles is developed to predict the detailed wave motions in the vicinity of the still waterline on a slope. The numerical method and the seaward and landward boundary algorithms are fairly general but the lateral boundary algorithm is limited to periodic boundary conditions. The computed results for surging waves on a rough 1:2.5 slope are presented for the incident wave angles in the range 0–80°. The time-averaged continuity, momentum and energy equations are used to check the accuracy of the numerical model as well as to examine the cross-shore variations of wave setup, return current, longshore current, momentum fluxes, energy fluxes and dissipation rates. The computed reflected waves and waterline oscillations are shown to have the same alongshore wavelength as the specified nonlinear incident waves. The computed variations of the reflected wave phase shift and wave runup are shown to be consistent with available empirical formulas. More quantitative comparisons will be required to evaluate the model accuracy.

ADDITIONAL INDEX WORDS: *Oblique waves, reflection, runup, revetments, breakwaters, wave setup, return current, longshore current.*

INTRODUCTION

BRUUN (1985, 1989) gave comprehensie reviews on the design and construction of rubble mound breakwaters. Experiments on inclined coastal structures conducted in directional wave basins are becoming more common throughout the world. These experiments were conducted mostly for straight structures on the horizontal bottom to examine the effects of incident wave angles and directionality on design variables such as wave runup (DE WALL and VAN DER MEER, 1992) and wave reflection (ISAACSON *et al.,* 1996). Available data are still limited partly because directional wave basin experiments include more design parameters and are much more time-consuming than unidirectional wave flume experiments. Furthermore, measurements are normally limited to free surface oscillations at several locations and do not provide detailed understanding of oblique wave dynamics on steep rough slopes.

Time-dependent numerical models for waves on inclined coastal structures are limited mostly to normally-incident waves as reviewed by KOBAYASHI (1995). LIU *et al.* (1995) solved the finite-amplitude, shallow-water equations numerically to predict solitary wave runup around a circular island with a 1:4 side slope. TITOV and SYNOLAKIS (1998) solved these equations numerically to predict the runup of tsunamis. On the other hand, KOBAYASHI and KARJADI (1996) and KOBAYASHI *et al.* (1997) developed numerical models for oblique irregular waves with small incident angles but these models cannot be used to examine the effects of incident wave angles on wave runup and reflection.

A two-dimensional, time-dependent numerical model for finite-amplitude, shallow-water waves with arbitrary incident angles is developed here to examine the effects of incident wave angles on oscillatory and time-averaged wave characteristics on a steep rough slope. As a first attempt, use is made of periodic lateral boundary conditions. Consequently, computations are limited to regular waves on a slope of alongshore uniformity. Incident nonlinear waves at the toe of the slope are specified as input to the model. Reflected waves are predicted at the toe of the slope to examine the height, shape, angle and phase shift of reflected waves as a function of the incident wave angle. Computed waterline oscillations are analyzed to obtain wave runup, setup and run-down as a function of the incident wave angle. The predicted wave reflection and runup are shown to be in agreement with available empirical formulas. In addition, the computed spatial and temporal variations of the free surface elevation and horizontal velocities are analyzed to elucidate the detailed wave mechanics on the steep rough slope.

NUMERICAL MODEL

The depth-integrated continuity and horizontal momentum equations in shallow water may be expressed as [*e.g.* LIU *et al.,* 1995]

98268 received 30 November 1998; accepted in received 12 February 2001.

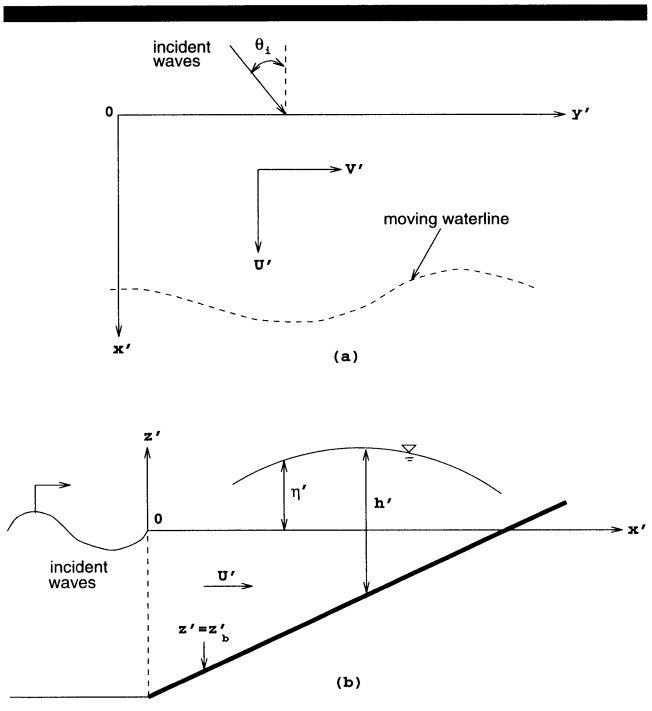

Figure 1. Definition sketch for dimensional variables.

$$\frac{\partial h'}{\partial t'} + \frac{\partial}{\partial x'}(h'U') + \frac{\partial}{\partial y'}(h'V') = 0 \tag{1}$$

$$\frac{\partial}{\partial t'}(h'U') + \frac{\partial}{\partial x'}(h'U'^2) + \frac{\partial}{\partial y'}(h'U'V') = -gh'\frac{\partial \eta'}{\partial x'} - \frac{1}{2}f_b'(U'^2 + V'^2)^{1/2}U' \tag{2}$$

$$\frac{\partial}{\partial t'}(h'V') + \frac{\partial}{\partial x'}(h'U'V') + \frac{\partial}{\partial y'}(h'V'^2) = -gh'\frac{\partial \eta'}{\partial y'} - \frac{1}{2}f_b'(U'^2 + V'^2)^{1/2}V' \tag{3}$$

where the prime indicates the physical variables; t' = time; x' = horizontal coordinate taken to be positive landward with $x' = 0$ at the toe of the slope as depicted in Figure 1; y' = horizontal coordinate parallel to the toe alignment and taken to be positive in the downwave direction; h' = water depth; U' = depth-averaged cross-shore velocity; V' = depth-averaged alongshore velocity; g = gravitational acceleration; η' = free surface elevation above the still water level (SWL); and f_b = bottom friction factor. The vertical coordinate z' is taken to be positive upward with $z' = 0$ at SWL as shown in Figure 1. The bottom elevation is located at $z' = z'_b$ where z'_b is negative below SWL. The spatial variation of z'_b is assumed to be known in the following.

The dimensional variables are normalized as

$$t = \frac{t'}{T'}; \quad x = \frac{x'}{\sigma H'}; \quad y = \frac{y'}{\sigma H'}; \quad U = \frac{U'}{\sqrt{gH'}}; \quad V = \frac{V'}{\sqrt{gH'}} \tag{4}$$

$$h = \frac{h'}{H'}; \quad \eta = \frac{\eta'}{H'}; \quad z_b = \frac{z_b'}{H'}; \quad f = \frac{1}{2}\sigma f_b'; \quad \sigma = \frac{T'\sqrt{gH'}}{H'} \tag{5}$$

where T' and H' = incident wave period and height, respectively, f = normalized bottom friction factor which is allowed to vary spatially; and σ = ratio of the horizontal and vertical length scales which is assumed to satisfy $\sigma^2 \gg 1$ in shallow water (*e.g.* KOBAYASHI and WURJANTO, 1992). Substituting Equations 4 and 5 into Equations 1–3, the normalized continuity and momentum equations are expressed in the conservative vector form:

$$\frac{\partial \mathbf{U}}{\partial t} + \frac{\partial \mathbf{E}}{\partial x} + \frac{\partial \mathbf{F}}{\partial y} + \mathbf{G} = 0 \tag{6}$$

with

$$\mathbf{U} = \begin{bmatrix} h \\ hU \\ hV \end{bmatrix}; \quad \mathbf{E} = \begin{bmatrix} hU \\ hU^2 + h^2/2 \\ hUV \end{bmatrix}; \quad \mathbf{F} = \begin{bmatrix} hV \\ hUV \\ hV^2 + h^2/2 \end{bmatrix};$$

$$\mathbf{G} = \begin{bmatrix} 0 \\ h\dfrac{\partial z_b}{\partial x} + f(U^2 + V^2)^{1/2}U \\ h\dfrac{\partial z_b}{\partial y} + f(U^2 + V^2)^{1/2}V \end{bmatrix} \tag{7}$$

where **E**, **F** and **G** depend on **U** only for given z_b and f. In the following, Equation 6 is solved numerically to compute the temporal and spatial variations of h, U and V. The mean water depth $\bar{h}$ and the mean velocities $\bar{U}$ and $\bar{V}$ are then obtained by time-averaging the computed h, U and V where the overbar indicates time-averaging.

To interpret the computed spatial variations of $\bar{h}$, $\bar{U}$, and $\bar{V}$, the time-averaged continuity and momentum equations are derived from Equation 6.

$$\frac{\partial}{\partial x}(\overline{hU}) + \frac{\partial}{\partial y}(\overline{hV}) = 0 \tag{8}$$

$$\frac{\partial}{\partial x}(S_{xx}) + \frac{\partial}{\partial y}(S_{xy}) = -\bar{h}\frac{\partial \bar{\eta}}{\partial x} - \tau_{bx} \tag{9}$$

$$\frac{\partial}{\partial x}(S_{xy}) + \frac{\partial}{\partial y}(S_{yy}) = -\bar{h}\frac{\partial \bar{\eta}}{\partial y} - \tau_{by} \tag{10}$$

with

$$S_{xx} = \overline{hU^2} + \frac{1}{2}\overline{(\eta - \bar{\eta})^2}; \quad S_{xy} = \overline{hUV}; \quad S_{yy} = \overline{hV^2} + \frac{1}{2}\overline{(\eta - \bar{\eta})^2} \tag{11}$$

$$\tau_{bx} = f\overline{(U^2 + V^2)^{1/2}U}; \quad \tau_{by} = f\overline{(U^2 + V^2)^{1/2}V} \tag{12}$$

where S_{xx}, S_{xy} and S_{yy} = time-averaged momentum fluxes similar to radiation stresses (LONGUET-HIGGINS, 1970); and τ_{bx} and τ_{by} = time-averaged bottom shear stress in the x and y-directions.

Expressing η, U and V with $h = (\eta - z_b)$ as the sum of the oscillatory and mean components and using linear progressive wave theory to describe the oscillatory components, Equations 8–10 can be reduced to the standard continuity and momentum equations used to predict the spatial variations of $\bar{\eta}$, $\bar{U}$ and $\bar{V}$ on beaches (*e.g.* WU and LIU, 1985). The assumption of linear progressive waves may not be valid for coastal structures because wave reflection may not be negligible. The accuracy of the time-dependent numerical model is checked using Equations 8–10 and 11–12 because the computed h, U and V using Equation 6 must satisfy the corresponding time-averaged equations.

The depth-integrated energy equation corresponding to Equations 1–3 can be derived from the three-dimensional continuity and momentum equations in shallow water (KOBAYASHI *et al.*, 1997) used to derive Equations 1–3 in the same way as the derivation of the one-dimensional energy equation from the two-dimensional continuity and momentum equations (KOBAYASHI and WURJANTO, 1992). The time-averaging normalized energy equation corresponding to Equation 6 may be expressed as

$$\frac{\partial}{\partial x}(F_x) + \frac{\partial}{\partial y}(F_y) = -D_f - D_B \tag{13}$$

with

$$F_x = \overline{hU\left[\eta + \frac{1}{2}(U^2 + V^2)\right]}; \qquad F_y = \overline{hV\left[\eta + \frac{1}{2}(U^2 + V^2)\right]};$$

$$D_f = \overline{f(U^2 + V^2)^{1.5}} \tag{14}$$

where F_x and F_y = time-averaged energy flux per unit width in the x and y-directions, respectively; and D_f and D_B = time-averaged rate of energy dissipation per unit horizontal area due to bottom friction and wave breaking, respectively. The dissipation rate D_B is related to the vertical variations of horizontal velocities and shear stresses outside the bottom boundary layer which are not predicted in this two-dimensional model. As a result, D_B is computed using Equations 13 and 14 for the computed h, U and V using Equation 6. The computed D_B must be positive or zero.

Various finite difference methods are available to solve Equation 6 (*e.g.* ANDERSON *et al.*, 1984). LIU *et al.* (1995) solved Equation 6 using a staggered explicit finite difference leap-frog scheme where the nonlinear convective terms were linearized with an upwind scheme of first order accuracy. Good agreement was obtained between the measured and computed free surface displacement and maximum runup around a circular island with a 1:4 side slope for nonbreaking solitary waves. They have noted that no numerical solution has been demonstrated to successfully reproduce wave breaking in a two-dimensional flow. Use is made here of the MacCormack method (MACCORMACK, 1969) which has been used successfully for the computation of two-dimensional transient open channel flows with bores (CHAUDHRY, 1993).

The finite difference grid of constant grid size Δx and Δy is used to solve Equation 6. The values of Δx and Δy must be small enough to resolve the rapid spatial variation of the wave motion on the slope. The nodes are located at $x = (i - 1)\Delta x$ with $i = 1, 2, \ldots, I$ and $y = (j - 1)\Delta y$ with $j = 1, 2, \ldots, J$ in Figure 1 where I and J = number of nodes in the x and y-directions, respectively. The landward boundary at $x = (I - 1)\Delta x$ is located above the moving waterline on the slope. The initial time $t = 0$ for the computation marching forward in time is taken to be the time when the incident wave train arrives at the seaward boundary $x = 0$ and there is no wave action in the computation domain. As a result, $\eta = 0$, $U = 0$ and $V = 0$ at $t = 0$. The waterline in the numerical model is defined as the location where the instantaneous water depth h equals a small value δ, which is taken as $\delta = 10^{-3}$ in the subsequent computation. The most landward wet node along the cross-shore line j is indicated by the integer s_j. For the dry nodes at $i = (s_j + 1), \ldots, I$, $h_{i,j} = 0$, $U_{i,j} = 0$ and $V_{i,j} = 0$ are set where the subscripts i and j indicate the nodal location.

For the known values of η, $h = (\eta - z_b)$, U and V at the time level t and at all the nodes used in the computation, the values of these variables at the next time level $t^* = (t + \Delta t)$, which are denoted by the superscript asterisk, are computed by solving Equation 6 using the MacCormack method, whose accuracy is second order in time and space. The predictor, corrector and final steps of the MacCormack method are expressed as

$$\dot{\mathbf{U}}_{i,j} = \mathbf{U}_{i,j} - \frac{\Delta t}{\Delta x}(\mathbf{E}_{i,j} - \mathbf{E}_{i-1,j}) - \frac{\Delta t}{\Delta y}(\mathbf{F}_{i,j} - \mathbf{F}_{i,j-1}) - \Delta t\mathbf{G}_{i,j} \tag{15}$$

$$\ddot{\mathbf{U}}_{i,j} = \dot{\mathbf{U}}_{i,j} - \frac{\Delta t}{\Delta x}(\dot{\mathbf{E}}_{i+1,j} - \dot{\mathbf{E}}_{i,j}) - \frac{\Delta t}{\Delta y}(\dot{\mathbf{F}}_{i,j+1} - \dot{\mathbf{F}}_{i,j}) - \Delta t\dot{\mathbf{G}}_{i,j} \tag{16}$$

$$\mathbf{U}^*_{i,j} = \frac{1}{2}(\mathbf{U}_{i,j} + \ddot{\mathbf{U}}_{i,j}) \tag{17}$$

which yields the values of η^*, $h^* = (\eta^* - z_b)$, U^* and V^* at the next time level t^* for the interior nodes.

The time step size Δt for each time step is determined using an approximate numerical stability criterion for the explicit finite difference method adopted in Equations 15–17. Slightly different criteria have been proposed as discussed by ANDERSON *et al.* (1984). Use is made here of that proposed by THOMPSON (1990) because of its simplicity

$$\Delta t = C_n / max\left[\frac{|U_{i,j}| + \sqrt{h_{i,j}}}{\Delta x} + \frac{|V_{i,j}| + \sqrt{h_{i,j}}}{\Delta y}\right] \tag{18}$$

where C_n = Courant number recommended to be in the range $C_n = 0.5$–1.0; and max = maximum value of the quantities in the square brackets at each node for all the nodes used in the computation. For the subsequent computation, the value of C_n less than unity specified as input is reduced to decrease Δt when numerical difficulties at the moving waterline occur.

The most landward wet node s^*_j along the cross-shore line j at the next time level t^* must be found to track the moving waterline where $s^*_j = (s_j - 1)$, s_j or $(s_j + 1)$ because of the numerical stability criterion given by Equation 18. The following simple procedure is adopted to compute $\mathbf{U}^*_{i,j}$ with $i = s_j$ and $(s_j + 1)$ using Equations 15–17. For $i = (s_j + 1)$ above

the waterline, $\mathbf{U}_{i,j} = \mathbf{0}$, $\mathbf{E}_{i,j} = \mathbf{0}$, $\mathbf{F}_{i,j} = \mathbf{0}$ and $\mathbf{G}_{i,j} = \mathbf{0}$ in Equation 15 where use is made of Equation 7. To compute $\dot{\mathbf{U}}_{i,j}$ with $i = (s_j + 1)$ using Equation 16, $(\dot{\mathbf{E}}_{i+1,j} - \dot{\mathbf{E}}_{i,j})$ is replaced by $(\dot{\mathbf{E}}_{i,j} - \dot{\mathbf{E}}_{i-1,j})$ for $i = (s_j + 1)$, corresponding to the linear extrapolation of $\dot{\mathbf{E}}_{i-1,j}$ and $\dot{\mathbf{E}}_{i,j}$ to estimate $\dot{\mathbf{E}}_{i+1,j}$. After $\mathbf{U}^*_{i,j}$ with $i = s_j$ and $(s_j + 1)$ is obtained using Equation 17, the value of s^*_j is found as follows: $s^*_j = (s_j - 1)$ if $h^*_{s_j,j} \leq \delta$; $s^*_j = s_j$ if $h^*_{(s_j+1),j} \leq \delta$; and $s^*_j = (s_j + 1)$ if $h^*_{(s_j+1),j} > \delta$. After s^*_j is obtained, $\mathbf{U}^*_{i,j} = \mathbf{0}$ with $i = (s^*_j + 1)$, ..., I is set for the dry nodes at the next time level.

The lateral boundaries of the numerical model are located along the cross-shore lines $j = 1$ and J where the bottom elevation z_b varies in the cross-shore direction. It is very difficult to specify incoming waves through the lateral boundaries into the computation domain and allow outgoing waves to propagate out of the computation domain without any numerical reflection from the lateral boundaries. As a first attempt, the periodic lateral boundary conditions are used here, although these conditions are appropriate only for regular waves on the slope of alongshore uniformity for which the bottom elevation z_b depends on x only in Figure 1. For the periodic lateral boundaries, the nodes along $j = 1$ and J can be treated as the interior nodes for which Equations 15–17 are written. To compute $\mathbf{U}^*_{i,j}$ with $j = 1$ and J using Equations 15–17, use is made of $\mathbf{F}_{i,0} = \mathbf{F}_{i,J-1}$ for $j = 1$ in Equation 15 and $\dot{\mathbf{F}}_{i,J+1} = \dot{\mathbf{F}}_{i,2}$ for $j = J$ in Equation 16.

The seaward boundary of the numerical model is located at the toe of the slope along the y-axis as shown in Figure 1. In the region $x \leq 0$, the bottom is assumed to be horizontal so that a regular wave theory on the horizontal bottom may be used to specify the normalized incident wave train $\eta_i(t,y)$ at $x = 0$ in the following form:

$$\eta_i(t,y) = F_i(p) \quad \text{at} \quad x = 0 \tag{19}$$

with

$$p = t - \lambda y; \qquad \lambda = \frac{T'\sqrt{gH'}}{L'}\sin\theta_i \tag{20}$$

where F_i = periodic function with respect to the phase p such that $F_i(p + 1) = F_i(p)$; L' = dimensional incident wavelength; θ_i = incident wave angle as shown in Figure 1; and λ = inverse of the normalized alongshore wavelength. The period T' and height H' of the incident wave train are used in Equations 4 and 5 to normalize the dimensional variables. Consequently, the period and height of η_i are unity. The alongshore wavelength, $L'/\sin\theta_i$, is constant on the slope of alongshore uniformity because of Snell's law (*e.g.* DEAN and DALRYMPLE, 1984). The function F_i depends on the wave theory used for a specific application. To satisfy the initial conditions of no wave action in the region $x \geq 0$, use is made of $\eta_i = tF_i$ for $0 \leq t < 1$ and $\eta_i = F_i$ for $t \geq 1$ where the computation is continued until the computed wave motion on the slope becomes periodic. To satisfy the periodic lateral boundary conditions, the computation domain width is taken as $0 \leq y \leq \lambda^{-1}$, which requires $(J - 1)\Delta y = \lambda^{-1}$.

The seaward boundary algorithm for obliquely incident and reflected waves is not well established because no unique direction of propagation for characteristic variables exists for multidimensional hyperbolic equations including Equation 6 (*e.g.* THOMPSON, 1990). VAN DONGEREN and SVENDSEN (1997) proposed an absorbing-generating algorithm for a two-dimensional, shallow-water model by extending the algorithm for the one-dimensional model proposed by KOBAYASHI *et al.* (1987). They tested their algorithm for unidirectional waves propagating in a domain of constant depth. Several algorithms including that of VAN DONGEREN and SVENDSEN (1997) were tried to produce the periodic wave motion on the slope which satisfies the time-averaged Equations 8–10. In addition, the computed reflected wave train must become periodic and propagate along the y-axis in a manner similar to Equation 19. The algorithm satisfying these requirements is presented in the following.

The continuity and x-momentum equations in Equation 6 are expressed in the following characteristic form:

$$\frac{\partial\alpha}{\partial t} + (U + C)\frac{\partial\alpha}{\partial x} + V\frac{\partial\alpha}{\partial y} = -C\frac{\partial V}{\partial y} - \frac{\partial z_b}{\partial x} - fh^{-1}(U^2 + V^2)^{1/2}U \tag{21}$$

$$\frac{\partial\beta}{\partial t} + (U - C)\frac{\partial\beta}{\partial x} + V\frac{\partial\beta}{\partial y} = -C\frac{\partial V}{\partial y} + \frac{\partial z_b}{\partial x} + fh^{-1}(U^2 + V^2)^{1/2}U \tag{22}$$

with

$$C = \sqrt{h}; \qquad \alpha = 2C + U; \qquad \beta = 2C - U \tag{23}$$

where C = normalized phase velocity in shallow water; and α and β = characteristic variables in the x-direction. Assuming $|U| < C$ in the vicinity of the seaward boundary, α and β represent the characteristics propagating landward and seaward, respectively. Since β propagates out of the computation domain, the following finite difference approximation of Equation 22 at $x = 0$ is used to compute $\beta^*_{1,j}$ with $i = 1$ at the seaward boundary:

$$\beta^*_{1,j} = \beta_{1,j} - \frac{\Delta t}{\Delta x}(U_{1,j} - C_{1,j})(\beta_{2,j} - \beta_{1,j}) - \frac{\Delta t}{2\Delta y}[V_{1,j}(\beta_{1,j+1} - \beta_{1,j-1}) + C_{1,j}(V_{1,j+1} - V_{1,j-1})] + \Delta t\left[\left(\frac{\partial z_b}{\partial x}\right)_{1,j} + f_{1,j}(h_{1,j})^{-1}(U^2_{1,j} + V^2_{1,j})^{1/2}U_{1,j}\right] \tag{24}$$

where $\beta_{1,0} = \beta_{1,J-1}$, $V_{1,0} = V_{1,J-1}$, $\beta_{1,J+1} = \beta_{1,2}$ and $V_{1,J+1} = V_{1,2}$ because of the periodic lateral boundary conditions assumed here. Equation 24 is used to compute $\beta^*_{1,j} = [2(h^*_{1,j})^{1/2} - U^*_{1,j}]$ for $j = 1, 2, \ldots, J$.

To find $h^*_{1,j}$ and $U^*_{1,j}$, an additional equation is necessary. The cross-shore velocity U_i associated with the incident wave train η_i specified by Equation 19 is estimated as $U_i = \eta_i\cos\theta_i/\sqrt{d}$ using linear shallow-water wave theory where d = still water depth at $x = 0$. The differences between the specified η_i and U_i and the computed η and U at $x = 0$ are assumed to satisfy the relationship for linear shallow-water waves propagating seaward

$$U - \frac{\eta_i\cos\theta_i}{\sqrt{d}} = -\frac{\eta - \eta_i}{\sqrt{d}} \quad \text{at } x = 0 \tag{25}$$

which is essentially the same as the relationship used in the one-dimensional model of KOBAYASHI *et al.* (1987). The use of Equation 25 for the present two-dimensional problem may seem inappropriate but the characteristic variable β involves $h = (d + \eta)$ and U only. Furthermore, PALMA and MATANO (1998) compared several open boundary conditions for an ocean circulation model and found the condition similar to Equation 25 promising. Equation 25 with $\beta = (2\sqrt{h} - U)$ yields

$$h = 2d + a - 2|d(a + d)|^{1/2} \quad \text{at } x = 0 \tag{26}$$

with

$$a = d + \sqrt{d}\beta + \eta_i(1 + \cos\theta_i) \quad \text{at } x = 0 \tag{27}$$

For the computed $\beta^*_{1,j}$, Equations 26 and 27 yield $h^*_{1,j}$ and $U^*_{1,j} = |2(h^*_{1,j})^{1/2} - \beta^*_{1,j}|$ with $j = 1, 2, \ldots, J$. Finally, the y-momentum equation 6 is used to compute $V^*_{1,j}$ with $j = 1, 2, \ldots, J$. Use is made of Equations 15–17 and the periodic lateral boundary conditions where $(\mathbf{E}_{1,j} - \mathbf{E}_{0,j})$ in Equation 15 is replaced by $(\mathbf{E}_{2,j} - \mathbf{E}_{1,j})$. This extrapolation is similar to that used by KOBAYASHI *et al.* (1997). Equations 16 and 17 yield $(hV)^*_{1,j}$ with $j = 1, 2, \ldots, J$ and then $V^*_{1,j} = (hV)^*_{1,j}/h^*_{1,j}$.

After $h^*_{i,j}$, $U^*_{i,j}$ and $V^*_{i,j}$ at all the nodes in the computation domain are computed, a smoothing procedure is applied to damp numerical high-frequency oscillations which may appear at the rear of the steep front of a breaking wave. Use is made here of the relatively simple procedure described in CHAUDHRY (1993) and modified by JOHNSON *et al.* (1996) to account for very small water depth near the moving waterline.

COMPUTED WAVE MOTIONS ON STEEP SLOPE

No appropriate data is available to verify the developed numerical model. This two-dimensional model becomes practically the same as the one-dimensional model of KOBAYASHI *et al.* (1987) for normally-incident waves which was compared with the large-scale riprap tests reported by AHRENS (1975). His test 12 is used as an example in the following. For this test, the riprap slope $\tan\theta = 0.4$; the still water depth at the toe of the 1:2.5 slope, $d' = 4.57$ m; the incident wave period $T' = 8.5$ s; the incident wave height $H' = 0.93$ m; the median mass of the riprap, $M_{50} = 35.4$ kg; and the density of the riprap, $\rho_a = 2710$ kg/m^3. The nominal diameter of the riprap defined as $D_{n50} = (M_{50}/\rho_a)^{1/3}$ was $D_{n50} = 0.236$ m. The test was limited to normally incident waves with $\theta_i = 0$. Computation is also made for the incident wave angle $\theta_i = 10°$, 20°, 30°, 40°, 50°, 60°, 70° and 80°.

For this test, $d'/H' = 4.9 \gtrsim 3$ and the effect of the toe depth on wave runup is secondary (KOBAYASHI *et al.*, 1987). The ratio σ of the horizontal and vertical length scales defined in Equation 5 is $\sigma = 28$ and the assumption of shallow water is appropriate. The surf similarity parameter given by $\xi = \sigma \tan\theta/\sqrt{2\pi}$ is $\xi = 4.4$ and the incident waves were observed to surge on the 1:2.5 slope (AHRENS and MCCARTNEY, 1975). The energy equation 13 will be used to examine the change of wave breaking intensity as function of the incident wave angle θ_i. The Ursell parameter $U_r = H'L'^2/d'^3$ is $U_r = 30 \gtrsim 26$ and cnoidal wave theory (*e.g.* DEAN and DALRYMPLE, 1984) is used to specify the incident wave profile in the same way as in the previous computation by KOBAYASHI *et al.* (1987). The cnoidal wavelength is $L' = 55.5$ m at the toe of the slope. The cnoidal wave profile corresponding to Equation 19 is expressed as

$$\eta_i(t, y) = \eta_{min} + cn^2[2K(t - \lambda y)] \tag{28}$$

where η_{min} = normalized trough elevation below SWL; cn = Jacobian elliptic function; and K = complete elliptic integral of the first kind. For this test, $K = 2.52$ and $\eta_{min} = -0.37$. The normalized crest elevation above SWL is 0.63, indicating that the specified incident wave profile is fairly nonlinear. The parameter λ is defined in Equation 20 and given by $\lambda = 0.463 \sin\theta_i$. The computation domain is taken as $0 \le x \le 0.71$ and $0 \le y \le \lambda^{-1}$ except for $\theta_i = 0$ because $\lambda = 0$ for $\theta_i = 0$. For $\theta_i = 0$, use is made of the value of λ corresponding to $\theta_i = 10°$. The number of nodes in the x and y-directions are taken as $I = J = 161$. The Courant number in Equation 18 is taken as $C_n = 0.3$ and the time step size Δt is on the order of 0.0004. The computed wave motion on the slope becomes periodic after a few wave periods. As a result, computation is made for $0 \le t \le 10$ and the time-averaging is performed for the last wave period $9 < t \le 10$.

The bottom friction factor f'_b used in Equations 2 and 3 needs to be specified as input. KOBAYASHI *et al.* (1987) used $f'_b = 0.3$ to obtain good agreement between the measured and predicted wave runup except for the slight overprediction for surging waves. CORNETT and MANSARD (1994) measured the shear stress on a rubble slope below SWL and showed that the measured friction factors were in fair agreement with the empirical formula developed by KAMPHUIS (1975) for rough turbulent oscillatory flow on a horizontal bottom. This formula yields $f'_b \simeq 0.5$ for this test where the amplitude of water particle orbits just outside the bottom boundary layer is assumed to be approximately $H'/2$. Consequently, $f'_b = 0.5$ is used here to improve the agreement between the measured and predicted wave runup for $\theta_i = 0$.

The computed results for the incident wave angles $\theta_i = 0$–80° are examined to ensure that the computed wave motions on the slope are periodic and satisfy the time-averaged equations Equations 8–10. In the following, the computed results for $\theta_i = 40°$ are presented as an example. The computed wave reflection and runup as a function of θ_i are then discussed in light of available empirical formulas.

Figure 2 shows the spatial variations of the free surface elevation η in the computation domain at time $t = 9$, 9.25, 9.5, 9.75 and 10. The computed spatial variations at $t = 9$ and 10 are identical because the periodicity is established before $t = 9$. In the region of no water with $h = (\eta - z_b) = 0$, use is made of $\eta = z_b$ to depict the bottom elevation z_b of the slope. Figure 2 indicates the oblique waves propagating along the slope. The computed waves on the 1:2.5 slope do not exhibit stem waves even for $\theta_i = 80°$ unlike waves propagating along vertical walls (*e.g.* YOON and LIU, 1989).

Figures 3–5 show the temporal variations of η, U and V, respectively, at $x = 0$, 0.13, 0.26, 0.40 and 0.53 along the cross-shore line at $y = 1.66$ where $\lambda^{-1} = 3.36$ for $\theta_i = 40°$. The waterline at SWL is located at $x = 0.445$. The lower limit

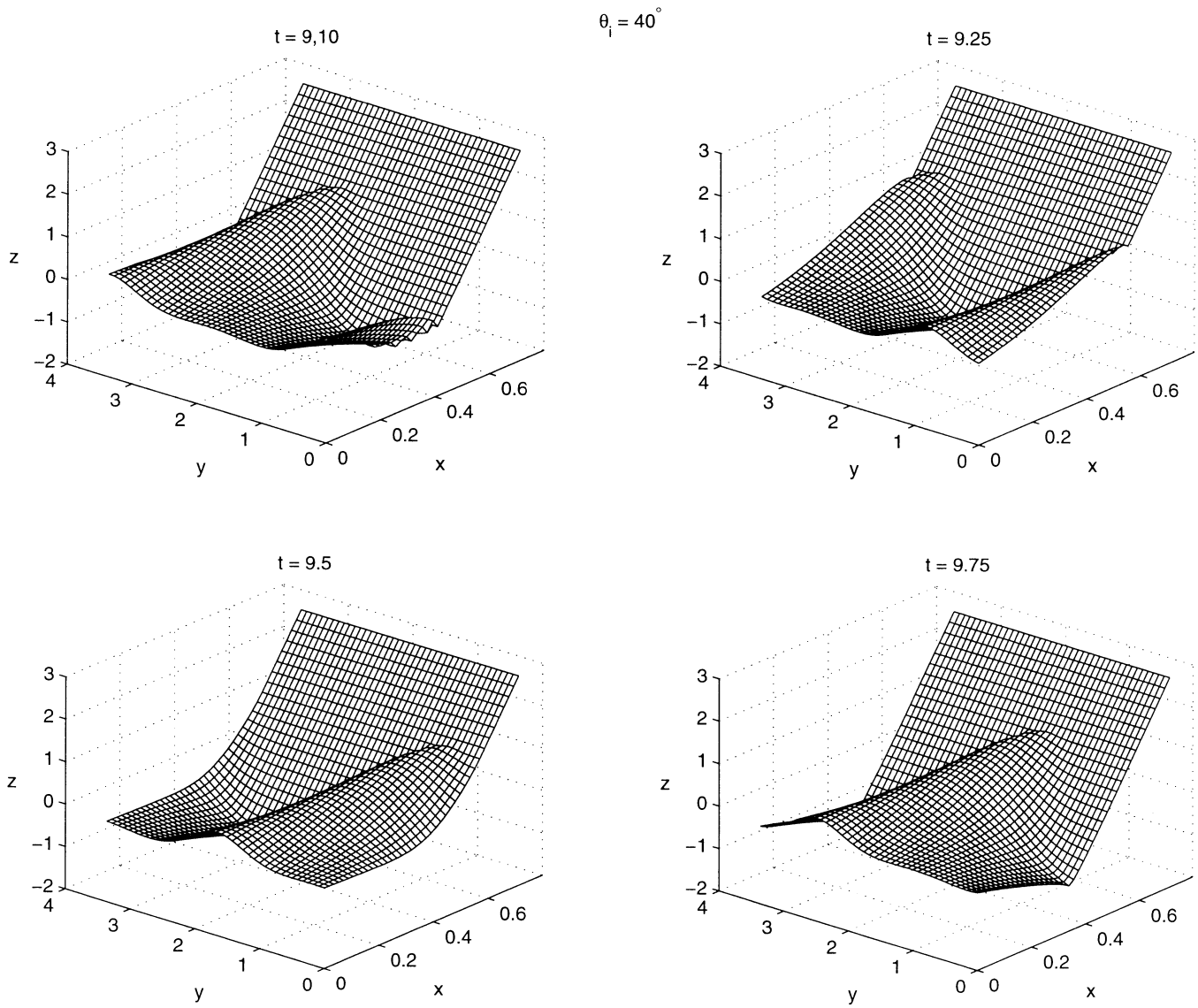

Figure 2. Spatial variations for free surface elevation η at time t = 9, 9.25, 9.5, 9.75 and 10.

of the free surface elevation η at $x = 0.40$ and 0.53 in Figure 3 corresponds to the bottom elevation $z_b = -0.49$ and 0.94, respectively. The effect of reflected waves is apparent in the trough of η at $x = 0$. The cross-shore velocity U at $x = 0.40$ and 0.53 in Figure 4 indicates wave uprush ($U > 0$) of a short duration and wave down-rush ($U < 0$) of a longer duration. The longshore velocity V at $x = 0.40$ and 0.53 in Figure 5 becomes more unidirectional ($V > 0$) because the large alongshore velocity occurs only during the short wave uprush. Figures 3–5 show that the computed wave motion becomes periodic after a few waves. The establishment of periodicity for the longshore velocity V on a gentle smooth slope is much slower as shown by KOBAYASHI and KARJADI (1994).

Figure 6 shows the cross-shore variations of the maximum, mean and minimum values of η, U and V during the last wave period $9 < t \leq 10$. The root-mean-square (rms) values of the oscillatory components $(\eta - \bar{\eta})$, $(U - \bar{U})$ and $(V - \bar{V})$ are also shown in Figure 6 to show the cross-shore variations of the oscillatory wave motion intensity. These rms values are the standard deviations of η, U and V. The quantities shown in Figure 6 are uniform alongshore. The 1:2.5 slope indicated by the solid straight line is added in the top panel to indicate the swash zone of wave uprush and down-rush on the slope. The rms wave intensity decreases landward in the swash zone but the largest velocities due to wave uprush occur slightly above the still waterline at $x = 0.455$. The wave setup $\bar{\eta}$ increases rapidly in the swash zone and approaches the upper limit of wave uprush. The mean cross-shore veloc-

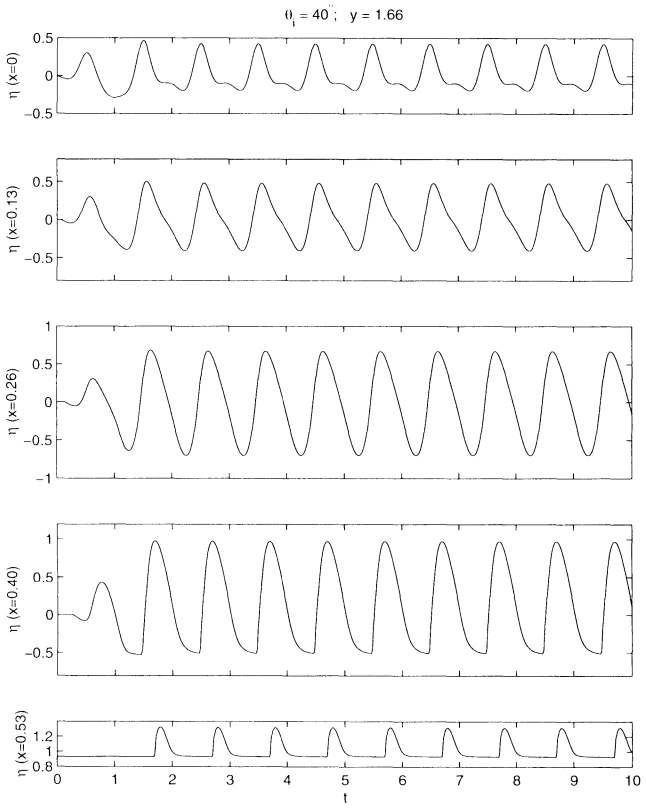

Figure 3. Temporal variations of η at five cross-shore locations.

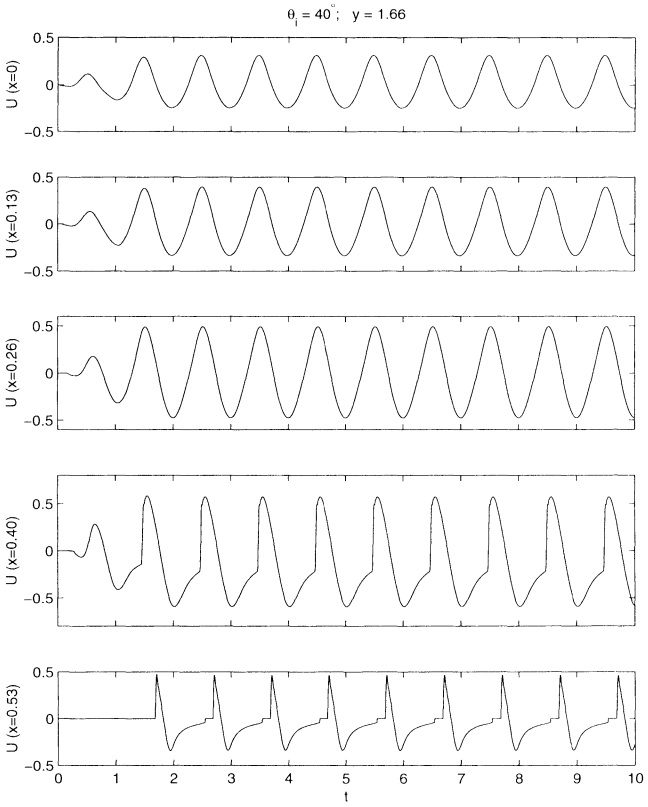

Figure 4. Temporal variations of cross-shore velocity U at five cross-shore locations.

ity $\bar{U}$ is negative and represents the cross-shore return current as explained by KOBAYASHI *et al.* (1989). The mean alongshore velocity $\bar{V}$ is the wave-induced longshore current which becomes almost as large as the standard deviation of V in the swash zone on the steep rough slope. The longshore current can become dominant on a gentle smooth slope (*e.g.* KOBAYASHI and KARJADI, 1994). It is noted that the computed value of $\bar{V}$ in the vicinity of $x = 0$ is slightly negative, indicating the minor shortcoming of the simple extrapolation used to compute $V^*_{1,J}$ as explained below Equation 27.

The computed spatial and temporal variations of η, U and V for the last wave period $9 < t \leq 10$ are used to compute the time-averaged quantities involved in Equations 8–10 and 13. The computed alongshore volume flux $\overline{hV}$ is uniform alongshore. The time-averaged continuity equation 8 requires $\overline{hU} = 0$ to satisfy the no flux condition into the impermeable slope. The computed cross-shore volume flux $\overline{hU}$ satisfies this requirement.

Figure 7 shows the cross-shore variations of the momentum fluxes S_{xx}, S_{xy} and S_{yy} and the bottom shear stresses τ_{bx} and τ_{by} involved in the time-averaged momentum equations 9 and 10 where the wave setup $\bar{\eta}$ is presented in Figure 6 and the mean water depth $\bar{h} = (\bar{\eta} - z_b)$. S_{xx} and S_{yy} increase landward and decrease in the swash zone, whereas S_{xy} is approximately constant seaward of the swash zone. The bottom shear stresses are important in the swash zone where the zone of $\tau_{bx} < 0$ and $\tau_{by} > 0$ corresponds approximately to the zone of $\bar{U} < 0$ and $\bar{V} > 0$ shown in Figure 6. The computed time-averaged quantities are uniform alongshore and satisfy the time averaged momentum equations 9 and 10. The negative cross-shore bottom shear stress τ_{bx} in Equation 9 increases wave setup $\bar{\eta}$ in the swash zone. The alongshore uniformity allows one to simplify Equation 10 as $\partial(S_{xy})/\partial x = -\tau_{by}$ which does not include time averaged dispersion or lateral mixing. This dispersion effect is important for longshore currents generated by regular breaking waves on gentle smooth slopes (KOBAYASHI *et al.*, 1997). No data on the longshore currents on steep rough slopes are available to evaluate the accuracy of the computed longshore current $\bar{V}$ shown in Figure 6 which indicates a fairly uniform profile in the swash zone unlike a triangular profile in the surf zone on a gentle slope predicted by a model without dispersion (KOBAYASHI *et al.*, 1997).

Figure 8 shows the cross-shore variations of the time-averaged energy fluxes F_x and F_y and the time-averaged energy dissipation rates D_f and D_B due to bottom friction and wave breaking, respectively. The computed values of these quantities are uniform alongshore. The time-averaged energy equation 13 is used to compute D_B which should be positive or zero. Figure 8 indicates that D_B is slightly negative in a narrow zone but that the energy dissipation for surging waves on this steep rough slope is dominated by the bottom friction. The cross-shore energy flux F_x decreases landward

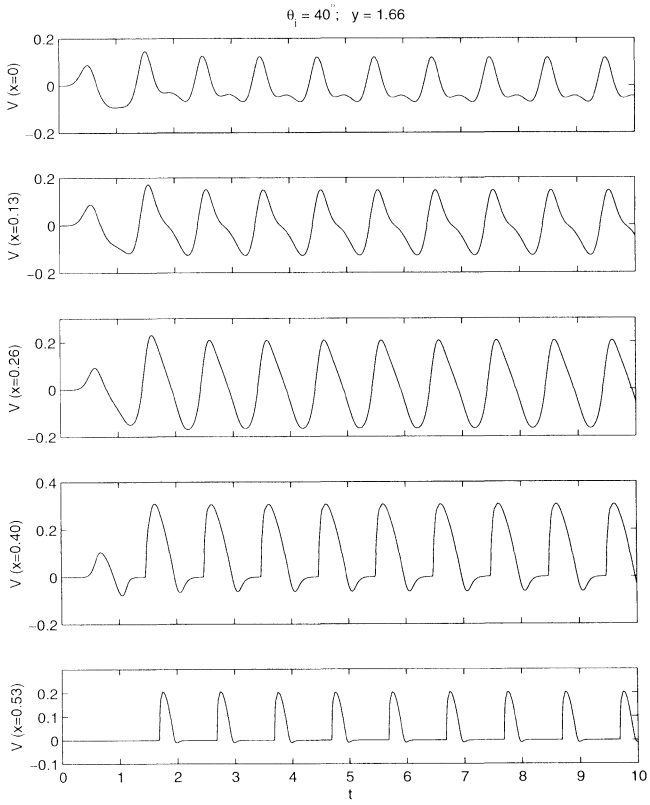

Figure 5. Temporal variations of longshore velocity V at five cross-shore locations.

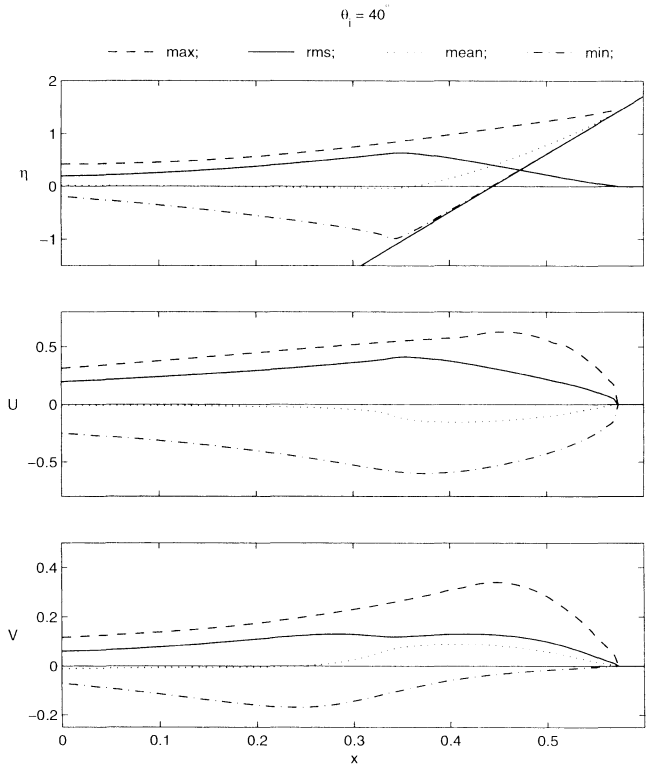

Figure 6. Cross-shore variations of maximum, root-mean-square, mean and minimum values of η, U and V.

mainly because of D_f which becomes the maximum near the still waterline. The alongshore energy flux F_y increases landward and decreases in the swash zone. It is noted that D_B turns out to be small in comparison to D_f for the entire range of θ_i = 0–80°. This implies that the intensity of wave breaking changes little even though the slope in the direction of incident wave propagation becomes gentler with the increase of θ_i.

The incident wave profile $\eta_i(t, y)$ along the seaward boundary $x = 0$ is specified as $\eta_i = tF_i$ for $0 \le t < 1$ and $\eta_i = F_i$ for $1 \le t \le 10$ as explained in relation to Equation 19 where F_i is given by Equation 28 for the assumed cnoidal wave profile. The periodic function F_i depends on $(t - \lambda y)$ with λ^{-1} = normalized alongshore wavelength where the computation domain is $0 \le \lambda y \le 1$. All the computed time series η_i at the 161 nodes along $x = 0$ for $0 \le t \le 10$ are plotted as a function of $p = (t - \lambda y)$ in Figure 9. The 161 time series do not coincide for $-1 \le p < 1$ in Figure 9 because of the adjustment of $\eta_i = tF_i$ for $0 \le t < 1$ to satisfy the initial conditions of no wave action in the computation domain. The reflected wave profile $\eta_r(t, y)$ along $x = 0$ is obtained as $\eta_r = (\eta - \eta_i)$ with η being the computed free surface elevation at $x = 0$. All the computed time series of η_r at the 161 nodes along $x = 0$ for $0 \le t \le 10$ are also plotted as a function of p in Figure 9. The reflected wave profile η_r becomes periodic with respect to p after a few waves. This implies that the alongshore wavelengths of the incident and reflected waves are the same where λ for the incident waves is defined in Equation 20. If the incident and reflected wavelengths are the same, $\sin \theta_i = \sin \theta_r$ where θ_r = reflected wave angle. This assumption is generally adopted to separate incident and reflected waves using linear wave theory (*e.g.* ISAACSON *et al.*, 1996).

The reflection coefficient r and the phase shift θ_r are estimated to examine their variations with respect to θ_i = 0–80°. The estimation of r and θ_r is based on the periodic portions of η_i and η_r shown in Figure 9 for $\theta_i = 40°$. The specified incident wave profile η_i is nonlinear where its crest and trough elevations are 0.63 and −0.37, respectively. The computed reflected wave profile η_r is more linear where the crest and trough elevations of η_r for $\theta_i = 40°$ are 0.27 and −0.22, respectively. To account for the profile difference, the reflection coefficient r is defined here as the ratio of the standard deviation of η_r to that of η_i. This reflection coefficient is slightly larger than the reflection coefficient based on the ratio of the reflected and incident wave heights. For $\theta_i = 40°$, $r = 0.50$ in comparison to the height ratio of 0.49. The phase shift ϕ_r is obtained here as the shift of the crests of the incident and reflected wave profiles plotted as a function of $(t - \lambda y)$. In Figure 9, $\phi_r = 0.47$ and the incident and reflected waves are out of phase.

Figure 10 shows the computed values of r and ϕ_r as a function of θ_i in degrees. The computed values of $r = 0.47$ for the normally-incident waves with $\theta_i = 0°$ is compared with avail-

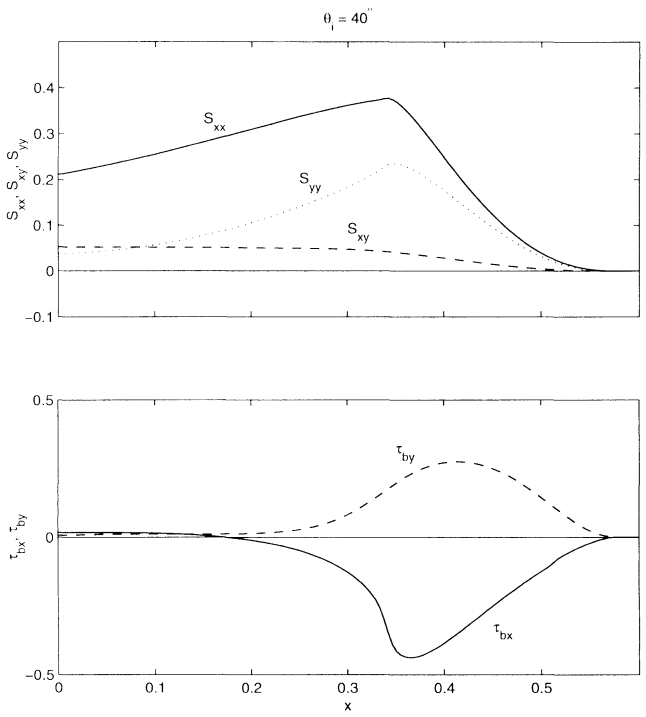

Figure 7. Cross-shore variations of time-averaged momentum quantities.

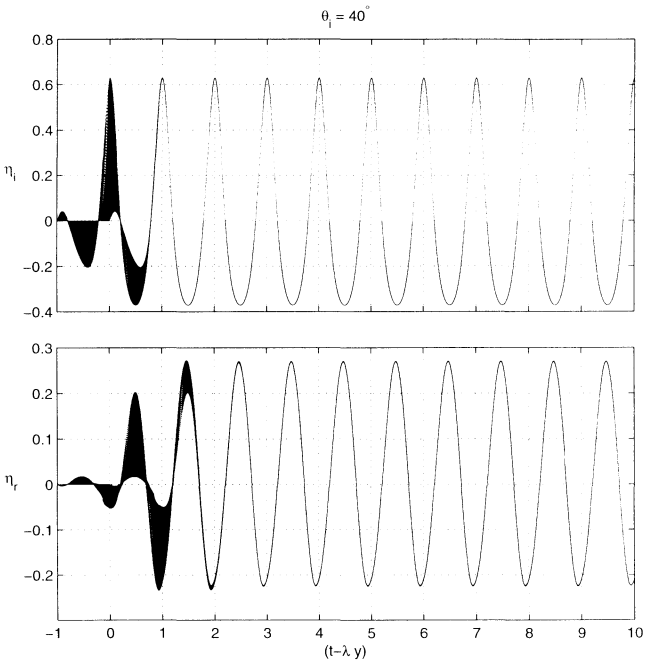

Figure 9. Incident and reflected wave profiles as a function of shifted time ($t - \lambda y$).

able empirical formulas. The formula of SEELIG and AHRENS (1995) predicts $r = 0.56$ for the rough impermeable slope assumed in the present computation. On the other hand, the formula of DAVIDSON *et al.* (1996) predicts $r = 0.41$. The difference between these empirical values is generally within the uncertainties associated with the empirical formulas and the linear wave theories used to estimate the measured reflection coefficients. The computed reflection coefficient r in Figure 10 increases from $r = 0.47$ for $\theta_i = 0°$ to $r = 0.59$ for $\theta_i = 80°$. Most of the regular wave data by ISAACSON *et al.*

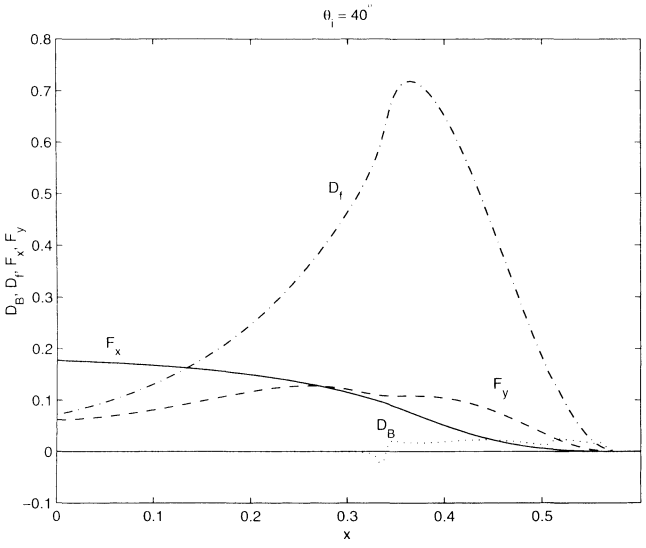

Figure 8. Cross-shore variations of time-averaged energy quantities.

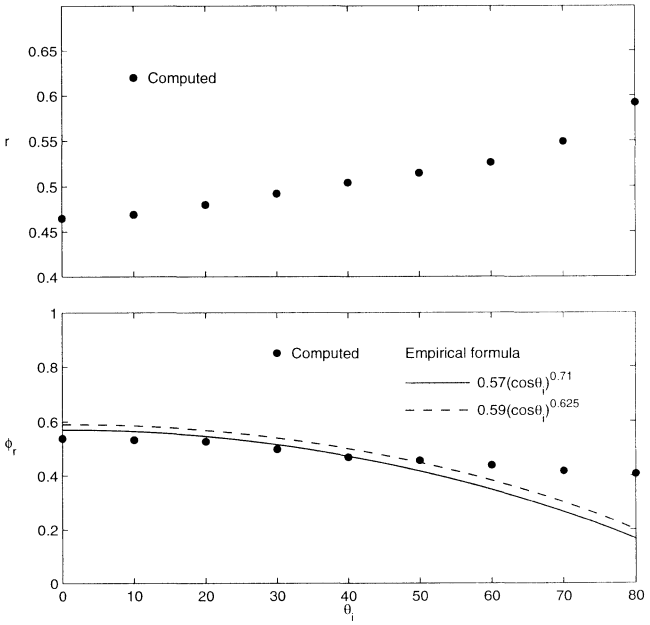

Figure 10. Reflection coefficient r and phase shift ϕ_r as a function of incident wave angle θ_i in degrees.

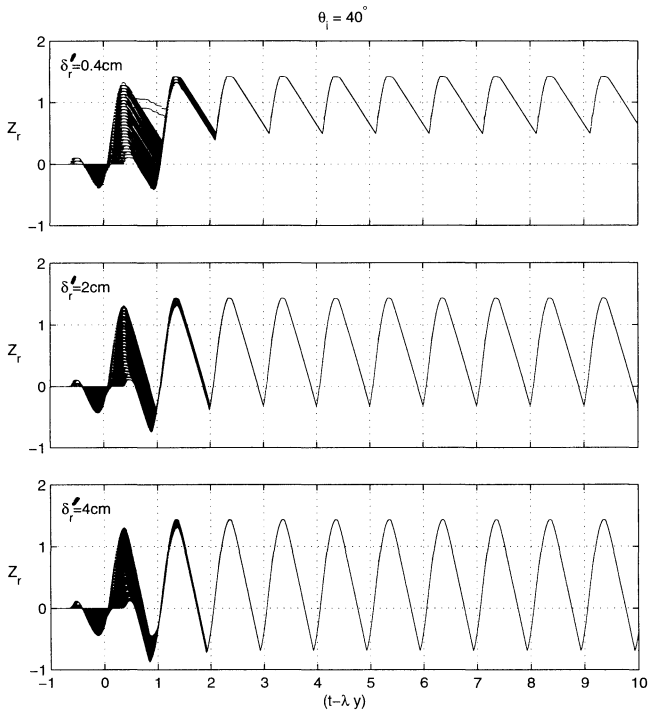

Figure 11. Waterline elevation Z_r for water depths δ'_r = 0.4, 2 and 4 *cm* as a function of shifted time ($t - \lambda y$).

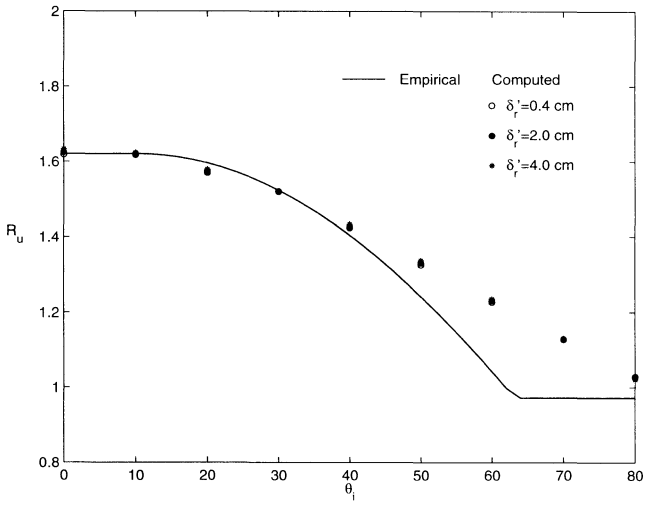

Figure 12. Wave runup R_u for δ'_r = 0.4, 2 and 4 *cm* as a function of θ_i in degrees.

(1996) indicated the increase of r with θ_i = 0 − 60°. As for the phase shift ϕ_r, SUTHERLAND and O'DONOGHUE (1998) proposed one empirical formula based on their data and another formula using their data and the data of HUGHES and FOWLER (1995) and ISAACSON *et al.* (1996). These formulas can be expressed as $\phi_r = 0.57(\cos\theta_i)^{0.71}$ and $\phi_r = 0.59(\cos\theta_i)^{0.625}$ for this specific case and are plotted in Figure 10. The agreement between the computed and empirical phase shifts is fair for the range $0 \le \theta_i \le 60°$ of the available data. Additional data for $\theta_i > 60°$ are required to assess the accuracy of the computed ϕ_r for $\theta_i > 60°$.

Finally, the computed waterline oscillations on the 1:2.5 slope are analyzed where the waterline elevation Z'_r above SWL is defined as the free surface elevation measured by a hypothetical wire placed at a vertical distance of δ'_r above the bottom and parallel to the slope in the cross-shore direction. Since the nominal stone diameter was 23.6 cm, use is made of δ'_r = 0.4, 2 and 4 cm which may represent the possible range of the roughness of the irregular bottom surface. For the actual computation, the normalized wire height $\delta_r = \delta'_r/H'$ with H' = 93 cm is used to compute the normalized waterline elevation $Z_r = Z'_r/H'$ above SWL as a function of t and y for the given δ_r.

All the computed time series of Z_r along the 161 cross-shore lines for $0 \le t \le 10$ are plotted as a function of $p = (t - \lambda y)$ for δ'_r = 0.4, 2 and 4 cm. The example for θ_i = 40° is shown in Figure 11. The computed waterline oscillations become periodic after a few waves. The normalized alongshore wavelength of the waterline oscillations on the slope is the same as the incident alongshore wavelength λ^{-1} at x = 0. This indicates the validity of Snell's law for obliquely incident waves on a slope of alongshore uniformity. Figure 11 shows that wave down-rush with a thin layer of water is sensitive to the wire height δ'_r.

The periodic portions of Z_r for δ'_r = 0.4, 2 and 4 cm as shown in Figure 11 for θ_i = 40° are used to obtain the maximum, mean, and standard deviation and minimum values of Z_r for θ_i = 0–80°. The maximum Z_r is the wave runup R_u which is shown in Figure 12. The wave runup R_u is not sensitive to δ'_r = 0.4–4 cm. The computed value of R_u for θ_i = 0° is 1.62 in comparison to R_u = 1.61 observed visually in his test 12 by AHRENS (1975). The empirical relationship shown in Figure 12 is based on the runup reduction factor $\gamma = R_u(\theta_i)/R_u(\theta_i = 0°)$ proposed by DE WALL and VAV DER MEER (1992). For unidirectional irregular waves, γ = 1 for $0° \le \theta_i \le 10°$, $\gamma = \cos(\theta_i - 10°)$ for $10° \le \theta_i \le 63°$, and γ = 0.6 for $63° \le \theta_i \le 80°$. The decrease of the computed regular wave runup with the increase of θ_i is represented fairly well by the empirical reduction factor for irregular wave runup except for θ_i = 60° and 70°. On the other hand, Figure 13 shows the wave runup R_u, the mean waterline elevation $\bar{Z}_r$, the standard deviation σ_r, and the wave run-down R_d, which is the minimum Z_r, for δ'_r = 2 cm. The computed R_u, $\bar{Z}_r$ and R_d decrease with the increase of θ_i, whereas the standard deviation of Z_r representing the intensity of the waterline oscillation about the mean $\bar{Z}_r$ remains approximately constant. Correspondingly, the value of $(R_u - R_d)$ remains approximately constant in Figure 13.

CONCLUSIONS

A two-dimensional, time-dependent numerical model for finite-amplitude, shallow water waves with arbitrary incident angles is developed to examine oblique wave dynamics on steep rough slopes. The use of periodic lateral boundary conditions has limited the present computations to regular

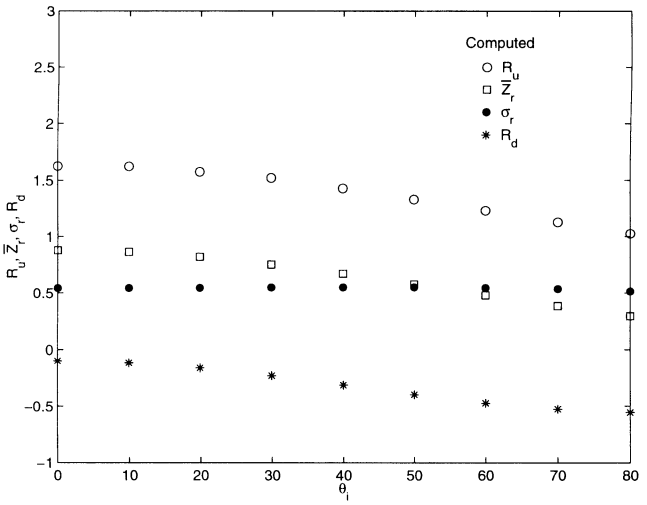

Figure 13. Wave runup R_u, setup $\bar{Z}_r$, standard deviation σ_r, and rundown R_d for $\delta'_r = 2\ cm$ as a function of θ_i in degrees.

waves on the slope of alongshore uniformity. The numerical method and the seaward and landward boundary algorithms presented here are general and expected to be applicable to irregular waves as well.

The computed spatial and temporal variations of the free surface elevation and the cross-shore and alongshore velocities are presented for surging waves on a rough 1:2.5 slope. The computed results for plunging waves on a rough 1:3.5 slope are similar except for the significant increase of the energy dissipation rate D_B in Figure 8 (KARJADI and KOBAYASHI, 1998). The utility of this numerical model is to obtain the detailed wave motions in the vicinity of the still waterline which are difficult to measure in experiments. The computed cross-shore and alongshore velocities become the maximum near the still water line. This is important for the evaluation of stone stability under obliquely incident waves. The computed longshore velocity becomes more unidirectional near the still water line. This suggests that the longshore transport of gravel or shingle may become the maximum near the still water line. The time-averaged continuity, momentum and energy equations are used to check the accuracy of the numerical model as well as to examine the spatial variations of the time-averaged quantities such as wave setup, return current, longshore current, momentum fluxes, energy fluxes and dissipation rates. The computed reflected waves and waterline oscillations are shown to have the same alongshore wavelength as the incident waves. This implies that the incident and reflected wave angles are the same even for nonlinear waves and that Snell's law is applicable even for steep rough slopes. The computed reflection coefficient r increases slightly with the increase of the incident wave angle θ_i, whereas the phase shift ϕ_r decreases slightly with the increase of θ_i. The computed wave runup R_u decreases with the increase of θ_i. These computed results are consistent with available experimental results.

ACKNOWLEDGMENT

This work was supported by the National Oceanic and Atmospheric Administration Office of Sea Grant, Department of Commerce, under Grant No. NA56RG0147 (Project SG97 R/OE-23).

LITERATURE CITED

AHRENS, J.P., 1975. Large wave tank tests of riprap stability. *Technical Memo No. 51,* U.S. Army Coastal Engineering Research Center, Ft. Belvoir, Virginia.

AHRENS, J.P. and MCCARTNEY, B.L., 1975. Wave period effect on the stability of riprap. *Proceedings, Civil Engineering in Ocean III,* New York,:ASCE, 2, 1019–1034.

ANDERSON, D.A.; TANNEHILL, J.C., and PLETCHER, R.A., 1984. *Computational Fluid Mechanics and Heat Transfer,* New York, NY: Hemisphere Publishing, 599p.

BRUUN, P., 1985. *Design and Construction of Mounds for Breakwaters and Coastal Protection,* New York, NY:Elsevier, 938p.

BRUUN, P., 1989. *Port Engineering,* 4th Edition, Houston, TX:Gulf Publishing, Volume 1, 1461p.

CHAUDHRY, M.N., 1993. *Open-Channel Flow,* Englewood Cliffs, NJ. Prentice Hall, 483p.

CORNETT, A. and MANSARD, E., 1994. Wave stresses on rubble-mound armor. *Proceedings, 24th Coastal Engineering Conference,* New York:ASCE, 1, 986–1000.

DAVIDSON, M.A.; BIRD, P.A.D.; HUNTLEY, D.A.; and BULLOCK, G.N., 1996. Prediction of wave reflection from rock structures: An integration of field & laboratory data. *Proceedings, 25th Coastal Engineering Conference,* New York, ASCE, 2, 2077–2086.

DEAN, R.G. and DALRYMPLE, R.A., 1984. *Water Wave Mechanics for Engineers and Scientists,* Englewood Cliffs, NJ:Prentice Hall, 353p.

DE WALL, J.P. and VAN DER MEER, J.W., 1992. Wave runup and overtopping on coastal structures. *Proceedings, 23rd Coastal Engineering Conference,* New York:ASCE, 2, 1758–1771.

HUGHES, S.A. and FOWLER, J.E., 1995. Estimating wave-induced kinematics at sloping structures. *Journal of Waterway, Port, Coastal, and Ocean Engineering,* ASCE, 121(4), 209–215.

ISAACSON, M.; PAPPS, D., and MANSARD, E., 1996. Oblique reflection characteristics of rubble-mound structures. *Journal of Waterway, Port, Coastal, and Ocean Engineering,* ASCE, 122(1), 1–7.

JOHNSON, B.D.; KOBAYASHI, N., and COX, D.T., 1996. Formulation and validation of vertically 2-D shallow-water wave model. *Proceedings, 25th Coastal Engineering Conference,* New York:ASCE, 1, 551–564.

KAMPHUIS, J.W., 1975. Friction factor under oscillatory waves. *Journal of Waterway, Port, Coastal, and Ocean Engineering,* ASCE, 101(2), 135–144.

KARJADI, E.A. and KOBAYASHI, N., 1998. Breaking waves and induced currents on coastal structures. *Proceedings, 26th Coastal Engineering Conference,* New York:ASCE, 1, 408–421.

KOBAYASHI, N., 1995. Numerical models for design of inclined coastal structures. *In*: KOBAYASHI, N. and DEMIRBILEK, Z. (eds.), *Wave Forces on Inclined and Vertical Wall Structures,* New York:ASCE, 118–138.

KOBAYASHI, N.; DESILVA, G.S., and WATSON, K.D., 1989. Wave transformation and swash oscillation on gentle and steep slopes. *Journal of Geophysical Research,* 94(C1), 951–966.

KOBAYASHI, N. and KARJADI, E.A., 1994. Swash dynamics under obliquely incident waves. *Proceedings, 24th Coastal Engineering Conference,* New York:ASCE, 2, 2155–2168.

KOBAYASHI, N. and KARJADI, E.A., 1996. Obliquely incident irregular waves in surf and swash zones. *Journal of Geophysical Research,* 101(C3), 6527–6542.

KOBAYASHI, N.; KARJADI, E.A., and JOHNSON, B.D., 1997. Dispersion effects on longshore currents in surf zones. *Journal of Waterway, Port, Coastal, and Ocean Engineering,* ASCE, 123(5), 240–248.

KOBAYASHI, N.; OTTA, A.K., and ROY, I., 1987. Wave reflection and

runup on rough slopes. *Journal of Waterway, Port, Coastal, and Ocean Engineering,* ASCE, 113(3), 282–298.

KOBAYASHI, N. and WURJANTO, A., 1992. Irregular wave setup and run-up on beaches. *Journal of Waterway, Port, Coastal, and Ocean Engineering,* ASCE, 118(4), 368–386.

LIU, P.L.-F.; CHO, Y.S.; BRIGGS, M.J.; KANOGLU, U., and SYNOLAKIS, C.E., 1995. Runup of solitary waves on a circular island. *Journal of Fluid Mechanics,* 302, 259–285.

LONGUET-HIGGINS, M.S., 1970. Longshore currents generated by obliquely incident sea waves. *Journal of Geophysical Research,* 75(33), 6778–6801.

MACCORMACK, R.W., 1969. The effects of viscosity in hypervelocity impact cratering. Pap. 69–354, *American Institute Aeronautics and Astronautics,* New York, NY.

PALMA, E.D. and MATANO, R.P., 1998. On the implementation of passive open boundary conditions for a general circulation model: The barotropic mode. *Journal Geophysical Research,* 103(C1), 1319–1341.

SEELIG, W.N. and AHRENS, J.P., 1995. Wave reflection and energy dissipation by coastal structures. *In*: KOBAYASHI, N. and DEMIRBILEK, Z. (eds.), *Wave Forces on Inclined and Vertical Wall Structures,* New York:ASCE, 28–51.

SUTHERLAND, J. and O'DONOGHUE, T., 1998. Wave phase shift at coastal structures. *Journal of Waterway, Port, Coastal and Ocean Engineering,* ASCE, 124(2), 90–98.

THOMPSON, K.W., 1990. Time-dependent boundary conditions for hyperbolic systems, II. *Journal of Computational Physics,* 89, 439–461.

TITOV, V.V. and SYNOLAKIS, C.E., 1998. Numerical modeling of tidal wave runup. *Journal of Waterway, Port, Coastal and Ocean Engineering,* ASCE, 124(4), 157–171.

VAN DONGEREN, A.R. and SVENDSEN, I.A., 1997. Absorbing-generating boundary condition for shallow water models. *Journal of Waterway, Port, Coastal, and Ocean Engineering,* ASCE, 123(6), 303–313.

WU, C.-S. and LIU, P.L.-F., 1985. Finite element modeling of nonlinear coastal currents. *Journal of Waterway, Port, Coastal, and Ocean Engineering,* ASCE, 111(2), 417–432.

YOON, S.B. and LIU, P.L.-F., 1989. Stem waves along breakwaters. *Journal of Waterway, Port, Coastal, and Ocean Engineering,* ASCE, 115(5), 635–648.